Optimizing transcranial ultrasound delivery at large incident angles by leveraging cranial leaky guided wave dispersion

Matteo Mazzotti [a,*], Eetu Kohtanen [b], Alper Erturk [b], Massimo Ruzzene [a]

[a] *P.M. Rady Department of Mechanical Engineering, University of Colorado Boulder, Boulder, USA*
[b] *G.W. Woodruff School of Mechanical Engineering, Georgia Institute of Technology, Atlanta, USA*

ARTICLE INFO

ABSTRACT

We investigate the role of leaky guided waves in transcranial ultrasound transmission in temporal and parietal bones at large incidence angles. Our numerical and experimental results show that the dispersion characteristics of the fundamental leaky guided wave mode with longitudinal polarization can be leveraged to estimate the critical angle above which efficient shear mode conversion takes place, and below which major transmission drops can be expected. Simulations that employ a numerical propagator matrix and a Semi-Analytical approach establish the transcranial dispersion characteristics and transmission coefficients at different incident angles. Experimental transmission tests conducted at 500 kHz and radiation tests performed in the 200–800 kHz range confirm the numerical findings in terms of transmitted peak pressure and frequency-radiation angle spectra, based on which the connection between critical angles, dispersion and transmission is demonstrated. Our results support the identification of transcranial ultrasound strategies that leverage shear mode conversion, which is less sensitive to phase aberrations compared to normal incidence ultrasound. These findings can also enable higher transmission rates in cranial bones with low porosity by leveraging dispersion information extracted through signal processing, without requiring measurement of geometric and mechanical properties of the cranial bone.

1. Introduction

In transcranial ultrasound operating with acoustic beams transmitted at normal incidence, the heterogeneous morphological and mechanical nature of the cranial bone is known to induce increasing refraction and phase aberration effects with increasing frequency. These effects reduce the efficiency of acoustic wave transmission and, due to large beam distortions occurring in the intracranial region, limit the spatial resolution achievable in imaging and brain stimulation [1]. Past studies [2–4] have demonstrated that these limitations can be mitigated by leveraging the conversion between longitudinal and shear bulk wave modes occurring at the bone–fluid interfaces. The use of shear mode conversion is attractive because the acoustic impedance mismatch between brain tissue, water and cranial bone is lower when the latter is sonicated at an incident angle higher than the first Snell's critical angle, which leads to lower distortions of the transmitted beam with respect to the normal incident case. This approach was employed for example in [2], where the transmission properties of a temporal bone for incident angles of up to 70° were investigated to demonstrate that, beyond the first Snell's critical angle, a reduction of the measured intracranial peak pressure was accompanied by a lower distortion of the transmitted acoustic beam. Other studies employed shear-to-longitudinal

mode conversion on parietal bones for the treatment of near-skull brain tissue [5], to characterize the so called "stripe artifact" in transcranial ultrasound through the temporal window [4], and to demonstrate that transmission data could be used to determine the acoustic properties of the cranial bone [3,6]. The latter are of paramount importance in the determination of Snell's critical angle and studies involving transcranial focused ultrasound (tFUS) [7–9], transducer modeling [1,10,11], as well as acoustic brain mapping [12] and imaging [13]. However, the skull acoustic properties are well known to display a large variability across different regions of the skull [14], and their estimation often requires *in vivo* complex procedures [15]. In addition, none of the works cited above consider a third mode conversion mechanism, namely the bulk-to-guided wave mode conversion. This mechanism plays a major role in transcranial ultrasound transmission, since guided waves generated within the sonicated cranial bone region at oblique incidence can re-radiate energy in the brain more or less efficiently in relation to the orientation of the acoustic beam. However, the evaluation of the radiation properties of leaky guided waves strongly depends on the accurate knowledge of the geometric and mechanical properties of the cranial bone, which makes their study and direct application rather difficult.

---

* Corresponding author.
  E-mail address: matteo.mazzotti@colorado.edu (M. Mazzotti).

Table 1
Mechanical properties of the temporal and parietal bones.

Bone		Geometric and mechanical properties							
		t (mm)	ρ (kg/m^3)	E (GPa)	v –	α_L (Np/(m MHz))	α_S (Np/(m MHz))	c_L (m/s)	c_S (m/s)
Temporal		3.47	1989	21.7	0.22	500.00	500.00	3529	2115
Parietal	Outer cortical	1.38	1944	14.7	0.25	160.00	320.00	3012	1739
	Trabecular	7.52	1211	5.70	0.35	240.00	360.00	2749	1320
	Inner cortical	1.55	1944	14.7	0.25	160.00	320.00	3012	1739

This work investigates the interplay between the conversion of guided wave modes and its role in transcranial ultrasound transmission in temporal and parietal bones. A first study investigating this phenomenon was conducted in [16], where it was numerically and experimentally demonstrated that angled transducers leveraging guided wave mode conversion can improve the transmission efficiency over the normal incidence case. Recently, cranial guided waves have emerged as a complementary tool to classic ultrasound for the study of the dispersive [17–19], mechanical [20] and radiation characteristics [21] of the human skull. Here, we demonstrate that frequency-dependent radiation properties of cranial leaky guided waves can be used to estimate the range of incident angles in which efficient shear mode conversion occurs. Specifically, we show that the first Snell's critical angle can be estimated with good accuracy by the radiation angle of leaky modes that exhibit a prevalent through-thickness longitudinal displacement polarization. In transmission tests performed on a temporal and a parietal bone, we observe that above this angle the transmitted acoustic beam suffers of lower distortions. For the temporal bone, we also observe that the transmission efficiency slightly increases with respect to the normal incident configuration, which indicates that the prior knowledge of this angle can be beneficial in experimental and clinical settings. The main advantage of using leaky guided waves in estimating this angle is that only simple signal processing procedures are needed to measure their dispersion properties. Therefore, the approach presented herein can potentially be employed in experimental or clinical settings to reduce the distortion of the transmitted acoustic beam in the intracranial region without any prior knowledge of the geometric and mechanical properties of the cranial bone.

2. Cranial bones

The analyses described in this work have been performed on the temporal bone of Fig. 1(a) and the parietal bone of Fig. 1(b), which were excised from two different human skulls from 60-year-old males of unknown medical history. The microcomputed tomographic (μCT) scan images of the two bones were obtained using a Scanco Medical μCT 50 scanner at 49.6 μm resolution, and were used to extract the average thickness of the cortical and trabecular layers necessary for the numerical analyses of Section 3. We note that although both bones measure approximately 94 mm in length, their total thickness varies from approximately 3.5 mm for the temporal bone to 11.00 mm for the parietal one. The mechanical properties of the bones are listed in Table 1. It is noted that these properties are only representative of the bone macroscopic mechanical behavior, which in turn implies that the operative wavelengths are not too small in comparison to the thickness of the bone layers. If the analyses are performed at high operative frequencies (very small wavelengths), other mechanical properties should be used that are more representative of the mechanical behavior of the bone at the microscopic level. Following [22], the mass density ρ (kg/m^3) of the cortical and trabecular layers were calculated by relating their corresponding volumes and Hounsfield Unit (HU) reconstructed from μCT images to the total measured mass (see Appendix A for additional details). The Young's modulus E (GPa) and Poisson's ratio (v) were obtained through experimental modal data using the approach and set up documented in [20,22], while the longitudinal and shear wave attenuation α_L and α_S (Np/(m MHz)) were obtained by fitting the transmission data obtained in Section 4.1. These properties are employed in Section 3 to numerically study the relation between transcranial transmission and guided wave mode conversion. However, it will be ultimately shown in Section 4.3 that such relation can be established in terms of dispersion properties of leaky guided modes, which can be obtained experimentally without any prior knowledge about the mechanical properties of the bone.

3. Numerical transmission analysis

This section describes the computational tools used in the transcranial ultrasound transmission analysis, namely the matrix propagator method and the Semi-Analytical Finite Element (SAFE) method. Both methods are based on the common assumption that propagating waves in water–bone–water systems as in Fig. 1(c) have the same wavenumber projection along the direction formed by the layers of the cranial bone (x-direction in Fig. 1(d)). In the matrix propagator method, this assumption is used to determine the directions along which bulk waves are progressively reflected and transmitted within each layer according to the generalized Snell's law, while in the SAFE method it enables the study of the dispersion properties of leaky guided wave modes [20,21]. The outputs from the two methods are, respectively, the transmission curves for varying incident angles at a given frequency and the frequency-dependent radiation angles of leaky guided wave modes propagating within the cranial bone. These will be used in Section 3.3 to interpret the experimental results of Section 4 in terms of relation between transcranial ultrasound transmission and mode conversion at the skull–fluid interface.

3.1. Transcranial ultrasound transmission estimation using the method of matrix propagator

To compute the frequency transmission curves for the water-cranial bone–water systems of Fig. 1(d), we consider the Brekhovskikh's method [23] with the corrections made in [24], based on which the cranial bone is idealized as the multilayered flat plate of Fig. 1(e). This is formed by different flat layers with parallel interfaces and infinite lateral extent. The two external layers are in contact with two water half spaces (density ρ_f = 1000 kg/m^3, phase speed c_f = 1480 m/s) that simulate the intracranial (brain) and extracranial (coupling medium) regions. The effects of the local curvature of the cranial bone on the transmitted acoustic beam are neglected since, in typical experimental settings, the local radius of curvature is generally much larger than the width of the acoustic beam impinging on the outer surface of the skull. The transmission coefficients are derived for the elasto-acoustic system sketched in Fig. 1(e), where the water half spaces and the three cranial layers, i.e. outer cortical, trabecular (diploë) and inner cortical, are labeled progressively as $l = 1, \ldots, 5$ along the z-direction (see Fig. 1(e)). The interface between two layers are labeled in a similar manner as $n = 1, \ldots, 4$. All the solid layers are assumed to be homogeneous and viscoelastic with material properties listed in Table 1. The thickness $t^{(l)}$ of each cranial layer was determined from the μCT images in Figs. 1(a) and (b) by averaging the local thickness t_p (see Fig. 1(d)) of the sonicated area of the cranial bone at a minimum of twenty locations. The total averaged thickness of the bone at such location is indicated as $H = \sum_l t^{(l)}$.
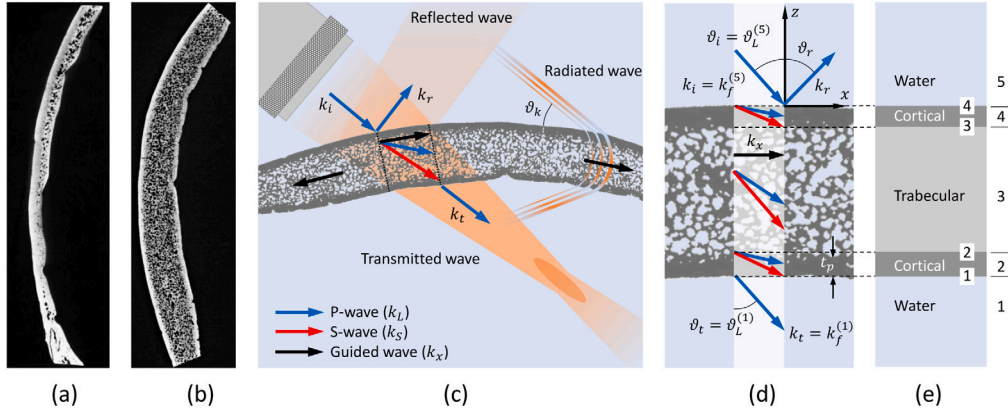
Fig. 1. (a) μCT scans of the (a) temporal and (b) parietal bone. (c) Transmission and wave guiding mechanisms in the cranial bone. (d) Detail of the cranial bone with the bulk and guided wave wavenumbers highlighted. (e) Equivalent system with parallel homogeneous viscoelastic layers used in the transmission and radiation calculations.

Following the analysis in [24], the amplitudes of the transmitted and reflected waves in the lower and upper water half spaces are computed for an incident monochromatic wave with radial frequency ω and a time-dependence of the form $\exp(-i\omega t)$ impinging on the outer cortical layer from the upper water half space at a given incident angle ϑ_i. In this work, ϑ_i is the main parameter used to determine the best transducer orientation for optimal transcranial ultrasound delivery. Since the generalized Snell's law is assumed to hold at any solid–solid and solid–liquid interface, the horizontal wavenumber $k_x = k_f \sin\vartheta_i = k_{L,S}^{(l)} \sin\vartheta_{L,S}^{(l)}$ is conserved within any layer and at any coordinate z. Here, $k_f = \omega/c_f$ is the fluid wavenumber in the upper water half space, while $k_{L,S}^{(l)} = \omega/c_{L,S}^{(l)}$ are the complex bulk wavenumbers of the longitudinal and shear bulk waves propagating within the lth layer at an angle $\sin\vartheta_{L,S}^{(l)}$ measured with respect to the z-direction. The complex longitudinal and shear phase speeds $c_{L,S}^{(l)}$ are computed as indicated in Appendix B. The conservation of k_x within each layer is used to derive the transmission ($T(\vartheta_i, \omega)$) and reflection ($R(\vartheta_i, \omega)$) coefficient by relating the particle velocity $\mathbf{v}^{(l)}(\vartheta_i, \omega) = \{v_x^{(l)}, v_z^{(l)}\}^T$ and impedance $\mathbf{Z}^{(l)}(\vartheta_i, \omega) = \{Z_x^{(l)}, Z_z^{(l)}\}^T$ (with $Z_{x,z}^{(l)} = \rho c_{S,L}^{(l-1)}$) at the interface between two adjacent layers l and $l-1$. For the equivalent fluid-loaded parietal bone system of Fig. 1(e), the recursive application of this procedure for all layers results in the following matrix relation [24]

$$\left\{ \begin{array}{c} \mathbf{v}^{(4)}(\vartheta_i, f) \\ \mathbf{Z}^{(4)}(\vartheta_i, f) \end{array} \right\} = \mathbf{A}(\vartheta_i, f) \left\{ \begin{array}{c} \mathbf{v}^{(1)}(\vartheta_i, f) \\ \mathbf{Z}^{(1)}(\vartheta_i, f) \end{array} \right\}, \tag{1}$$

where $\mathbf{A} = \prod_2^{l-1} \mathbf{S}^{(l)} = \mathbf{S}^{(4)}\mathbf{S}^{(3)}\mathbf{S}^{(2)}$ denotes the global matrix propagator for the three-layered parietal bone, in which the sixteen analytical coefficients $\mathbf{S}^{(l)}(\vartheta_i, \omega) = [s_{ij}^{(l)}(\vartheta_i, \omega)]$ ($i, j = 1, \ldots, 4$) for the lth layer are given in Appendix B. The transmission and reflection coefficients in the lower and upper water half space can be expressed as a function of the coefficients $A_{ij}(\vartheta_i, \omega)$ ($i, j = 1, \ldots, 4$), and read as [24]

$$T(\vartheta_i, f) = \frac{2Z^{(1)}}{(M_{22} + Z^{(1)}M_{23})Z^{(5)} + M_{32} + Z^{(1)}M_{33}}, \tag{2}$$

$$R(\vartheta_i, f) = \frac{M_{32} + Z^{(1)}M_{33} - (M_{22} + Z^{(1)}M_{23})Z^{(5)}}{M_{32} + Z^{(1)}M_{33} + (M_{22} + Z^{(1)}M_{23})Z^{(5)}}, \tag{3}$$

in which

$$M_{22} = A_{22} - A_{21}A_{42}A_{41}^{-1}, \quad M_{23} = A_{23} - A_{21}A_{43}A_{41}^{-1}, \tag{4}$$

$$M_{32} = A_{32} - A_{31}A_{42}A_{41}^{-1}, \quad M_{33} = A_{33} - A_{31}A_{43}A_{41}^{-1}. \tag{5}$$

For the case of the temporal bone, the matrix propagator reduces to $\mathbf{A} = \mathbf{S}^{(2)}$, with the layers 1 and 3 being the lower and upper water half spaces, respectively. Eq. (2) allows to compute the transmission coefficient $T(\vartheta_i, f)$ for the water–bone–water system for any given incident angle ϑ_i and frequency f. It should be noted that since each layer is modeled as a continuous and homogeneous plate, the

scattering effects induced by porosity are not explicitly accounted for, and they are rather included in the model by considering equivalent viscoelastic material coefficients evaluated from experimental data. While the above assumption does not pose significant limitations on the applicability of the method to temporal bones at frequencies below 2.0 MHz, for parietal bones the method can potentially lead to inaccurate results at frequencies for which the wavelength of the shear waves within the diploë are substantially smaller than the average size of the trabeculae. In addition, the matrix propagator method is known to suffer of low accuracy at very low values of the frequency-thickness product, for which wavelengths are usually expected to be much larger than the thickness of the layers. These constraints limit the applicability of this approach to operative frequencies larger than 200 kHz and lower than 1.0 MHz for the parietal bone. At higher frequencies, the wavenumber k_x is no longer expected to be conserved within each layer, and surface modes confined within the cortical bones are likely to form as observed in [18,20].

3.2. Cranial leaky guided wave dispersion using SAFE

Although the transmission analysis described in Section 3.1 is based on the conservation of the horizontal wavenumber k_x within each layer, it does not explicitly show the effect of leaky guided wave modes in the transmission coefficients. As already demonstrated in [18,19,21,25,26], cranial leaky guided waves can form and propagate within the cranial layer in certain frequency–wavenumber (f, k_x) ranges. However, since the frequency and radiation angle are two independent quantities when the mechanical and acoustical characteristics of the fluid-loaded bone are fixed, the solutions for $k_x(f)$ when f is a real valued parameter (time-transient guided waves) differ from the solutions $f(k_x)$ when k_x is a real valued parameter (steady leaky guided waves) [27]. In principle, these solutions can be extracted from the determinant of the propagator matrix $\mathbf{A}(\vartheta_i, f)$, although this operation results in a nonlinear eigenvalue problem that involves the definition of specific Riemann sheets in the complex plane $\mathrm{Re}(k_x(f)), \mathrm{Im}(k_x(f))$ on which physical solutions lie (see [28–31] for more details). This computational issue can be circumvented as described in Appendix C, where transformation techniques based on a Semi-Analytical Finite Element (SAFE) approach [21,32] are described that allow to transform a nonlinear eigenvalue problem into a linear polynomial one for both the $k_x(f)$ and $f(k_x)$ formulations. The output of both formulations is an eigenset $(f_k, k_{x,k}, \boldsymbol{\Phi}_k)$, where k denotes the kth guided wave mode supported by the cranial bone and $\boldsymbol{\Phi}_k$ indicates its corresponding through-thickness displacement profile. From the computed eigensets, the radiation angle of the kth guided wave mode at a given frequency is obtained from the generalized Snell's law $\vartheta_k = \sin^{-1}\left[\mathrm{Re}(k_{x,k})/k_f\right]$. As demonstrated in [27], the loci of transmission maxima in the $f-\vartheta$ spectrum computed
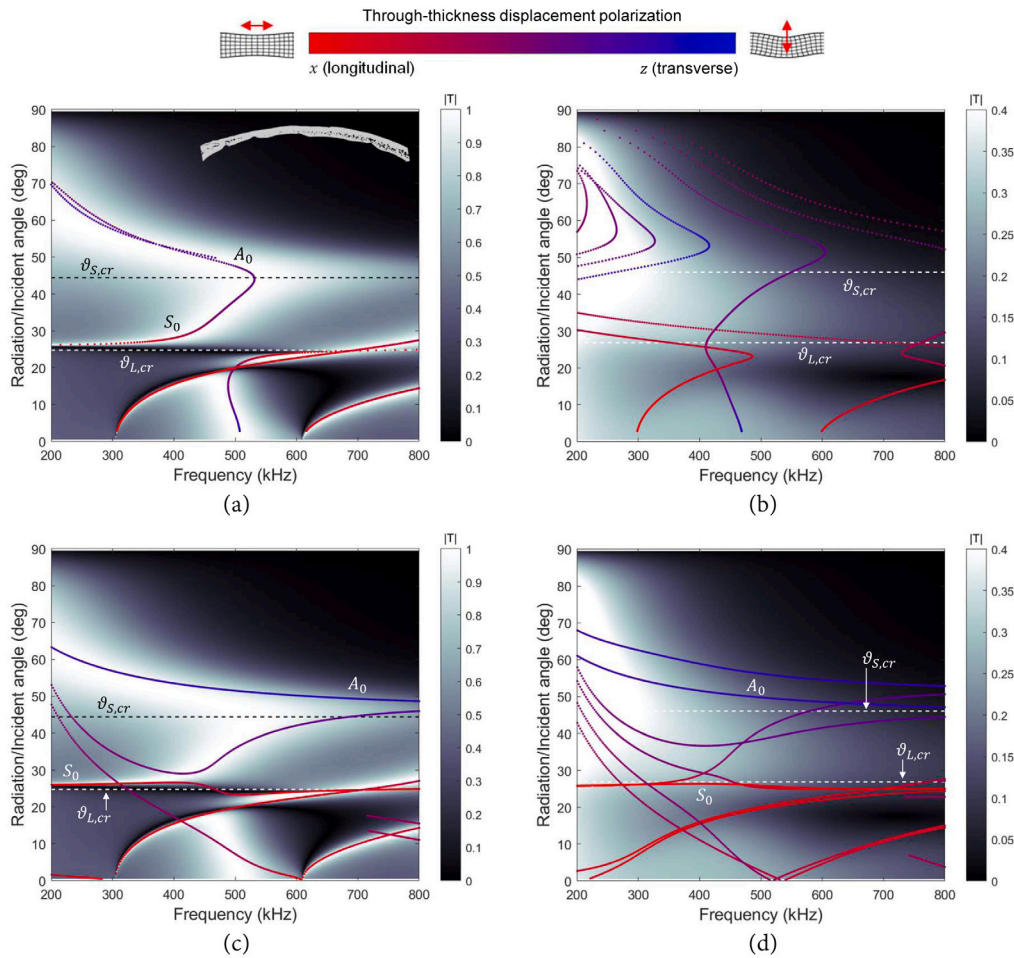
Fig. 2. Numerical maps of the transmission coefficient $|T(\vartheta_i, f)|$ for the temporal bone of Fig. 1(a) with superimposed $f(k_x)$ dispersion curves for the (a) elastic and (b) viscoelastic case, and with superimposed $k_x(f)$ dispersion curves the (c) elastic and (d) viscoelastic case. The $f(k_x)$ curves are generally associated with loci of maximum transmission, while the $k_x(f)$ curves of S_0 (red) and A_0 (blue) modes approximate the first ($\vartheta_{L,cr}$) and second ($\vartheta_{S,cr}$) critical angle, respectively.

using the matrix propagator approach of Section 3.1 correspond to the dispersion curves obtained from the $f(k_x)$ formulation for a one layer plate, such as the temporal bone. This is because the $f(k_x)$ formulation assumes that guided waves generated within the sonicated area of the bone vary in time and not in space when following a phase front, i.e. their spatial attenuation is null. In a physical setup, this condition can only be attained when the excitation signal is limited in time and the transducer width-to-bone thickness ratio is very large, which approximately corresponds to the assumption of incident monochromatic waves made in Section 3.1. When the source is more localized in space and the excitation signal is harmonic, time-steady leaky guided waves are generated and the $k_x(f)$ formulation is more appropriate. However, in this case some modifications would need to be introduced in the computation of the transmission coefficients as described in [33–35], where the finite width of the source is taken into account. Nonetheless, in this work the assumptions made in Section 3.1 were still found to provide reasonably accurate results. In addition, in the next Section it will be shown that the coincidence between loci of transmission maxima and the dispersion curves generated using the $f(k_x)$ formulation is still lost for the parietal bone at small radiation angles (large wavelengths), and that the $k_x(f)$ formulation can be more useful in identifying the critical angles and regions of optimal shear mode conversion for both bones when large material attenuation values are taken into account.

3.3. Transcranial ultrasound transmission analysis

In the following, we analyze qualitatively the relation between transcranial ultrasound transmission efficiency and leaky guided wave modes for the temporal and parietal bones by using the numerical methods of Sections 3.1 and 3.2. The numerical transmission and dispersion analyses are performed by considering the geometric and mechanical properties listed in Table 1. In order to evaluate the effects of attenuation, we also differentiate between the ideal case in which the cranial bone is perfectly elastic and the more realistic viscoelastic case.

3.3.1. Temporal bone

The elastic and viscoelastic results for the temporal bone are shown in Fig. 2. Since in this case the bone can be idealized as a single-layered, homogeneous plate, the Cremer's coincidence principle [27, 36,37] applies, based on which total transmission of sound through a perfectly elastic plate, i.e. $|T|^2 = 1$ and $|R|^2 = 0$, is achieved when the fluid impedance $Z_f = \rho_f c_f$ is substantially lower than the plate impedance $Z_L = \rho c_L$. Considering typical values of the mechanical parameters of water-loaded temporal bones ($\rho \in [1500, 2500]$ kg/m^3, $c_L \in [2500, 3500]$ m/s [2–4]), this condition usually holds with good approximation in the elastic regime, and therefore nearly total transmission can be expected when $\vartheta_i(f) \approx \vartheta_k(f)$ ($k = 1, 2, ..$). This scenario can be observed in Fig. 2(a), where dispersion curves obtained from

the $f(k_x)$ and $k_x(f)$ formulations are overlapped with the transmission maps computed from Eq. (2) for the elastic case. The dispersion curves are color coded depending on their through-thickness displacement polarization, and classified between longitudinally polarized and transversally polarized modes. The two fundamental symmetric and antisymmetric modes whose dispersion curves can be tracked back to the axis of null frequency are denoted in Fig. 2 as S_0 and A_0, respectively. For the temporal bone, the through-thickness profile of longitudinally polarized modes is symmetric with respect to the mid surface of the plate itself, while transversally polarized modes exhibit an antisymmetric profile. The polarization factor $PF_k(f)$ used to encode the curves is computed as indicated in Appendix C. From Fig. 2(a), it can be observed that the loci of curves (ϑ_i, f) determined by transmission maxima correspond, according to Cremer's coincidence condition and the analysis in [27], to the radiation dispersion curves obtained from the $f(k_x)$ formulation. However, this coincidence is not verified everywhere when the dispersion curves obtained using the $k_x(f)$ formulation (Fig. 2(c)) are considered. Therefore, the experimental measurement of time-transient leaky guided waves ($f(k_x)$) instead of standing leaky guided waves ($k_x(f)$) would allow to evaluate the regions of the spectrum $f - \vartheta_i$ in which high transmission values can be achieved. However, when moving from the elastic case of Fig. 2(a) to the viscoelastic case of Fig. 2(b), it can be inferred that the coincidence between loci of transmission maxima and dispersion curves is generally lost. Note that, in this case, at frequencies larger than 400 kHz the transmission coefficient drops in the interval $\vartheta_i \in [15°, 25°]$, and grows in the $\vartheta_i \in [25°, 45°]$ interval, where it reaches values similar to those relative to quasi-normal incidence ($\vartheta_i \in [0°, 10°]$). Here, it can be observed that the highest transmission rate at large incident angles is verified in the range defined by $\vartheta_{L,cr}$ and $\vartheta_{S,cr} = \sin^{-1}[c_f/\mathrm{Re}(c_S)]$ (second critical angle). This behavior is consistent with that observed in [2], in which the largest drop in transmission for a viscoelastic temporal bone analyzed at 740 kHz was found to take place at about 5° less than the first critical angle. The two critical angles are indicated in Fig. 2 with a dashed line and can be used to have an indirect measure of the region of the $f - \vartheta_i$ spectrum where optimal shear mode conversion is achieved. To this end, the $f(k_x)$ formulation cannot provide useful information since there are no dispersion branches that approach these angles, with the modes S_0 and A_0 merging in the 400–530 kHz range and becoming purely imaginary at frequencies larger than 530 kHz, using the $f(k_x)$ formulation. On the other hand, if the $k_x(f)$ formulation is used, then the two fundamental modes (S_0) and antisymmetric (A_0) define a pair of virtual boundaries that envelopes the region of high transmission at oblique incidence, with the first remaining very close to $\vartheta_{L,cr}$ across the whole frequency range and the latter approaching asymptotically $\vartheta_{S,cr}$ at high frequencies.

The qualitative analyses discussed above lead to the main conclusion that transmission via shear mode conversion in temporal bones can be efficiently achieved in the range $\vartheta_i \in [\vartheta_{L,cr}, \vartheta_{S,cr}]$. As observed in [2,3], operating in this range comes with the added benefit of lower distortions induced on the transmitted acoustic beam, which is due to a better impedance match at the water–bone–water interfaces and consequently to a lower phase alteration with respect to the normal incidence case, in which both longitudinal and shear waves are converted. However, the knowledge of the above interval is strictly related to the knowledge of the longitudinal and shear wave speed in the cranial bone, which can vary substantially in different regions of the cranial vault. Since $\vartheta_{L,cr} \approx \vartheta_{S0}$ and $\vartheta_{S,cr} \approx \vartheta_{A0}$ at moderate to high frequencies, the radiation dispersion curves of the fundamental symmetric and antisymmetric guided wave modes can be alternatively used to determine such interval. The benefit of using the dispersion curves lies in the fact that they can be obtained via pure signal processing, thus not requiring the knowledge of the geometric and mechanical properties of the cranial bone. This conclusion is verified in Sections 4 and 4.3 by means of experimental tests.

3.3.2. Parietal bone

The transmission properties of the parietal bone can be qualitatively analyzed in view of the observations made in Section 3.3.1 for the temporal bone. The corresponding $f - \vartheta$ spectra are reported in Fig. 3. Unlike the case of the elastic temporal bone, in the elastic parietal bone analyzed with the $f(k_a)$ formulation (Fig. 3(a)) and the $k_x(f)$ formulation (Fig. 3(c)), the coincidence between transmission maxima and dispersion branches is observed only for $\vartheta_i > 30°$, where the through-thickness displacement polarization of different leaky guided wave modes is neither purely longitudinal nor purely transversal. Below this angle, the different leaky guided modes display a prevalent longitudinal polarization. In the $k_x(f)$ elastic and viscoelastic dispersion spectra of Figs. 3(c, d), the dispersion branches of the longitudinally polarized modes form a cluster that is closely focused at a radiation angle approximately equal to 30°. This angle can be approximately identified as the first critical angle of the parietal bone. The cluster defining such angle, which is not clearly observed in the $f(k_x)$ spectra of Figs. 3(a, b), virtually separates regions of the $f - \vartheta_i$ spectrum characterized by high and low transmission. In general, the highest transmission values are observed at incident angles smaller than that defined by the cluster, except at frequencies lower than 250 kHz, where high transmission rates can be reached for up to $\vartheta_i \approx 45°$. It is interesting to note that, in the 550–750 kHz range, normal incidence leads to transmission values that are significantly smaller than those achieved at the $\vartheta_i \in [20°, 30°]$. In addition, it is also possible to note the presence of a second cluster of modes in the $k_x(f)$ dispersion spectra that departs near $\vartheta = 75°$ at 200 kHz and reaches a value of $\vartheta = 65°$ at 800 kHz. This cluster appears to play a significant role only in the elastic case, where it defines a virtual boundary above which high transmission can only be expected for incident beams that are narrowly focused at incident angles defined by the different dispersion branches. In the viscoelastic case, this cluster falls on a region of low transmission that holds no interest for practical applications. Therefore, the experimental measurement of the first cluster in the parietal bone is sufficient to determine the loci of the spectrum where transmission drops and lower distortions of the transmitted acoustic beam are likely to be expected. As can be deduced from Fig. 3(d), the former and the latter tend to distribute at 5°–10° below and above the first cluster, respectively.

4. Experimental investigation of transmission and radiation

This Section focuses on the experimental detection of the transmission coefficients and radiation angles of leaky guided waves predicted using the numerical approaches of Sections 3.1 and 3.2. The transmission and radiation experimental tests were performed for the degassed temporal and parietal bones using the immersed setup shown in Fig. 4. While the excitation of bulk and leaky guided waves differs for the two types of tests, the signal acquisition is performed in the same manner as described in the following. In both tests, the pressure field is scanned over a rectangular area by means of a needle hydrophone attached to a servomotor-operated stage. The hydrophone (Teledyne Reson TC 4038, diameter: 4 mm, receiving sensitivity: 50–800 kHz, nominal receiving sensitivity: -226 ± 3 dB re 1V/μPa at 500 kHz) has a flat frequency response and is connected through a preamplifier (Stanford Research Systems SR560) to a digital oscilloscope (HandyScope HS3). As indicated in Fig. 4(a), the 2D scan area covered with the hydrophone measures 120 mm in height (x_1-direction) and 100 mm in width (x_2-direction), and is discretized into a grid of 0.25 mm spatial step in each direction. At each point of the grid, the pressure field is recorded for 500 μs with a 10.0 MHz sampling rate. The 2D scan region lies on the plane that orthogonally intersects the two cranial bones at approximately half their width. Wave diffraction phenomena from the edges of the cranial bone are considered to be negligible since diffracted waves propagate in the surrounding fluid with semi-circular wavefronts, and therefore their amplitude attenuates rapidly due to spherical spreading. In both tests, bulk and Lamb waves are excited using an ultrasonic immersion transducer (Olympus V391-SU, diameter: 28.58 mm, center frequency: 0.47 MHz, peak frequency: 0.46 MHz, -6 dB bandwidth: 61.47 %).
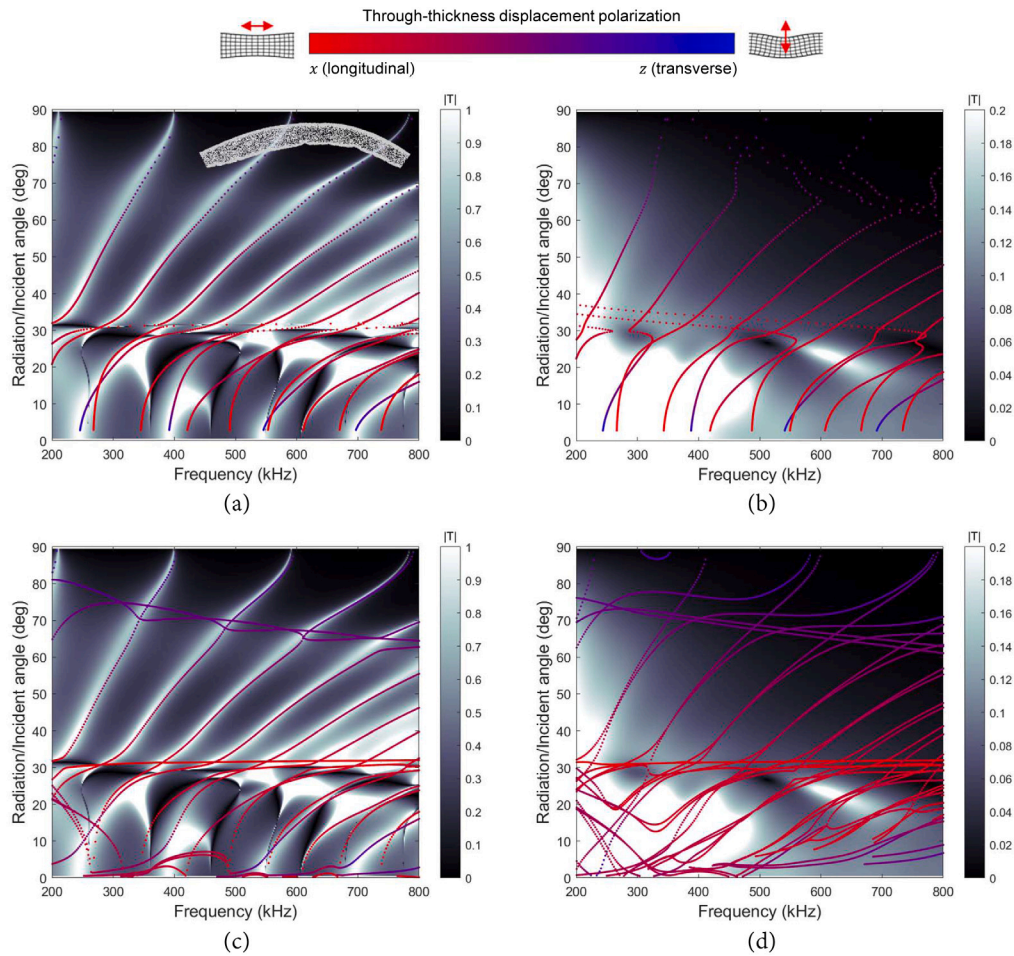
Fig. 3. Numerical maps of the transmission coefficient $|T(\vartheta_i, f)|$ for the parietal bone of Fig. 1(b) with superimposed $f(k_x)$ dispersion curves for the (a) elastic and (b) viscoelastic case, and with superimposed $k_x(f)$ dispersion curves the (c) elastic and (d) viscoelastic case. The $k_x(f)$ dispersion curves of guided wave modes with longitudinal through-thickness polarization (red) form a cluster at about $30°$. Below this angle, the coincidence between dispersion curves and loci of maximum transmission in generally lost.
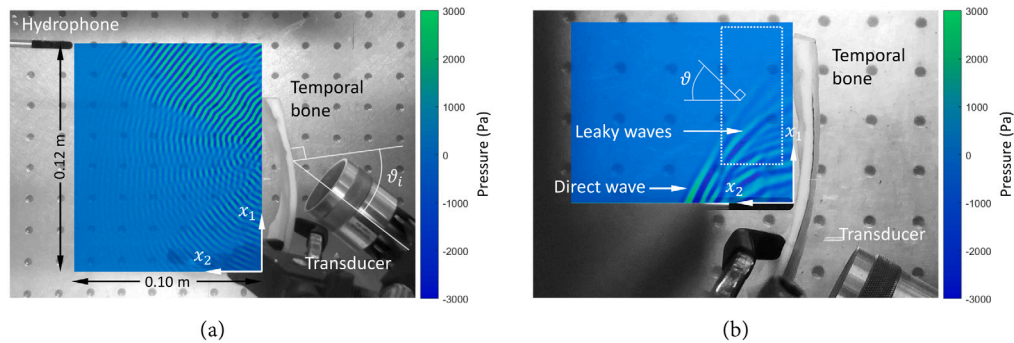
Fig. 4. Experimental setup with time snapshots of the pressure distribution for the (a) transmission and (b) dispersion tests performed on the temporal bone of Fig. 1(a).

4.1. Transmission tests

In the transmission test (Fig. 4(a)), the transducer was excited with a 50-cycle Gaussian-modulated sine wave of 500 kHz center frequency by means of a commercial signal generator (HP 33120 A) and a piezoelectric amplifier (Khron-Hite 7500). The transducer was positioned close to the center of each cranial bone using a 3D printed inclined spacer. Different spacers were printed for incident angles ϑ_i varying from $0°$ to $45°$ degrees at steps of $2.5°$. For all the incident angles, the gap between the cranial bone and the center of the face of the transducer was approximately 15 mm. This design choice was dictated by the fact that, at the operative frequency of 500 kHz, the measured focal distance

(position of last axial maxima) of the transducer in the free field setup (Fig. 7(a)) is 63 mm. Therefore, the close proximity between transducer and cranial bone ensures that the focal point of the transmitted field is always contained within the 2D scan window (intracranial region). With the above setup, the experimental peak transmission coefficients are computed as

$$T^{(p)}(f, \vartheta_i) = \frac{\left| \bar{p}(x_1^{(p)}, x_2^{(p)}, f, \vartheta_i) \right|}{\left| \bar{p}_0(x_1^{(p)}, x_2^{(p)}, f) \right|}, \tag{6}$$

where $\bar{p}(x_1, x_2, f, \vartheta_i)$ indicates the time Fourier transform of the transmitted pressure field $p(x_1, x_2, t, \vartheta_i)$ for a given incident angle ϑ_i of
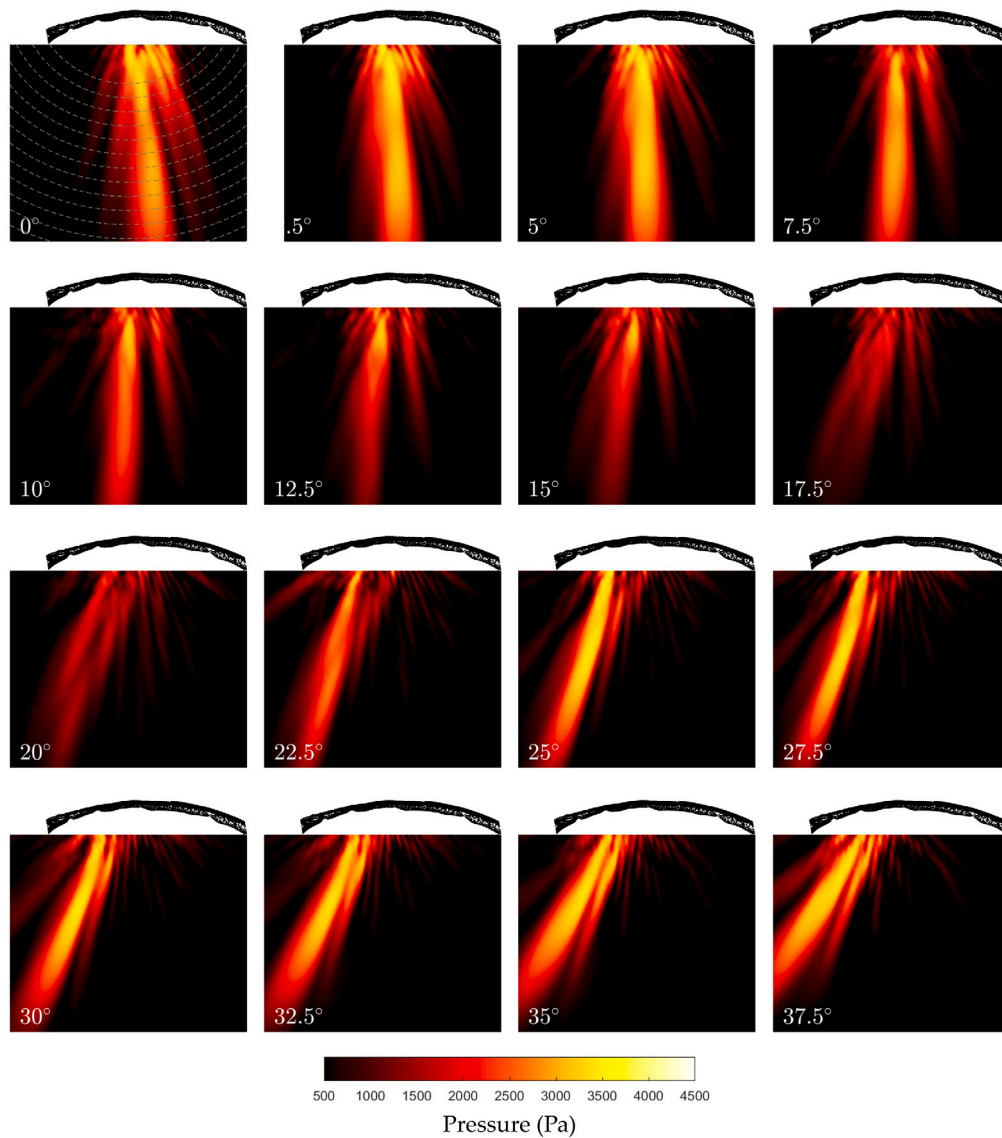
Fig. 5. Root Mean Square (RMS) maps of the experimental pressure field $p(x_1, x_2, t)$ for the temporal bone of Fig. 1(a).

the transducer, while $(x_1^{(p)}, x_2^{(p)})$ are the coordinates at which the peak pressure is observed. If the bone geometry does not induce significant aberration, then $(x_1^{(p)}, x_2^{(p)})$ correspond to the coordinates of the focal point in presence of the cranial bone. In this case, it should be noted that the focal length changes with respect to the free field setup. The peak pressure at the focal point in the free field is indicated with $\bar{p}_0(x_1^{(p)}, x_2^{(p)}, f)$, and is used in Eq. (6) to normalize the transmission coefficient. The Root Mean Square (RMS) maps of the recorded pressure fields for the temporal and parietal boned are given in Figs. 5 and 6, respectively. From these maps, it is possible to quantify the distortion induced on the transmitted acoustic beam by the cranial bone with respect to the free field case. To do so, two reference parameters are first extracted from the RMS map of the free field case at 500 kHz (Fig. 7(a)), namely the reference beam area A_f and the averaged reference beam width W_f. These quantities are computed by first normalizing the RMS map to unity and then taking the acoustic pressure contours corresponding to the -6 dB threshold. The reference beam area A_f is then computed as the area enclosed by such contours, while the averaged reference beam width W_f is evaluated as the average width of the beam contours measured across different interpolated trajectories (indicated with light dashed lines in Fig. 7(a)). The same operations are repeated on the RMS maps of Figs. 5 and 6, from which the angle-dependent beam area $A_b(\vartheta)$ and average beam width $W_b(\vartheta)$ are obtained

in presence of the cranial bones. The interpolation trajectories used to evaluate $A_b(\vartheta)$ and $W_b(\vartheta)$ are shown in Figs. 5 and 6 only for the $\vartheta = 0°$ case, and are not repeated in the remaining plots for ease of visualization. The amount of distortion induced by the bones on the transmitted acoustic beam with respect to the free field case is evaluated by means of two metrics, namely the beam area distortion ratio $\psi_A(\vartheta) = A_b(\vartheta)/A_f - 1$ and the beam width distortion ratio $\psi_W(\vartheta) = W_b(\vartheta)/W_f - 1$. The beam area distortion ratio $\psi_A(\vartheta)$ is shown in Fig. 7(b) for the temporal (solid line) and parietal bone (dashed line). As it can be observed this parameter is negative across the range $\vartheta \in [0°, 40°]$ for both bones, thus indicating that the area of the acoustic beam subtended by the -6 dB threshold is smaller than the corresponding area in the free field case for both cranial bones. The overall trend, however, is slightly different for the two bones. Specifically, in the case of the temporal bone, a slightly lower beam area distortion is observed with respect to the normal incident case in the range $\vartheta \in [25°, 30°]$, as also confirmed by the behavior of $\psi_W(\vartheta)$ in Fig. 7(c). On the other hand, the behavior of $\psi_A(\vartheta)$ and $\psi_W(\vartheta)$ for the parietal bone indicates a much lower beam distortion for incident angles larger than 27.5°, which is clearly observable in the RMS maps of Fig. 6. Interestingly, the average width of the transmitted acoustic beam in the $\vartheta \in [27.5°, 37.5°]$ range is also up to 25% smaller than that of the free field case. This behavior
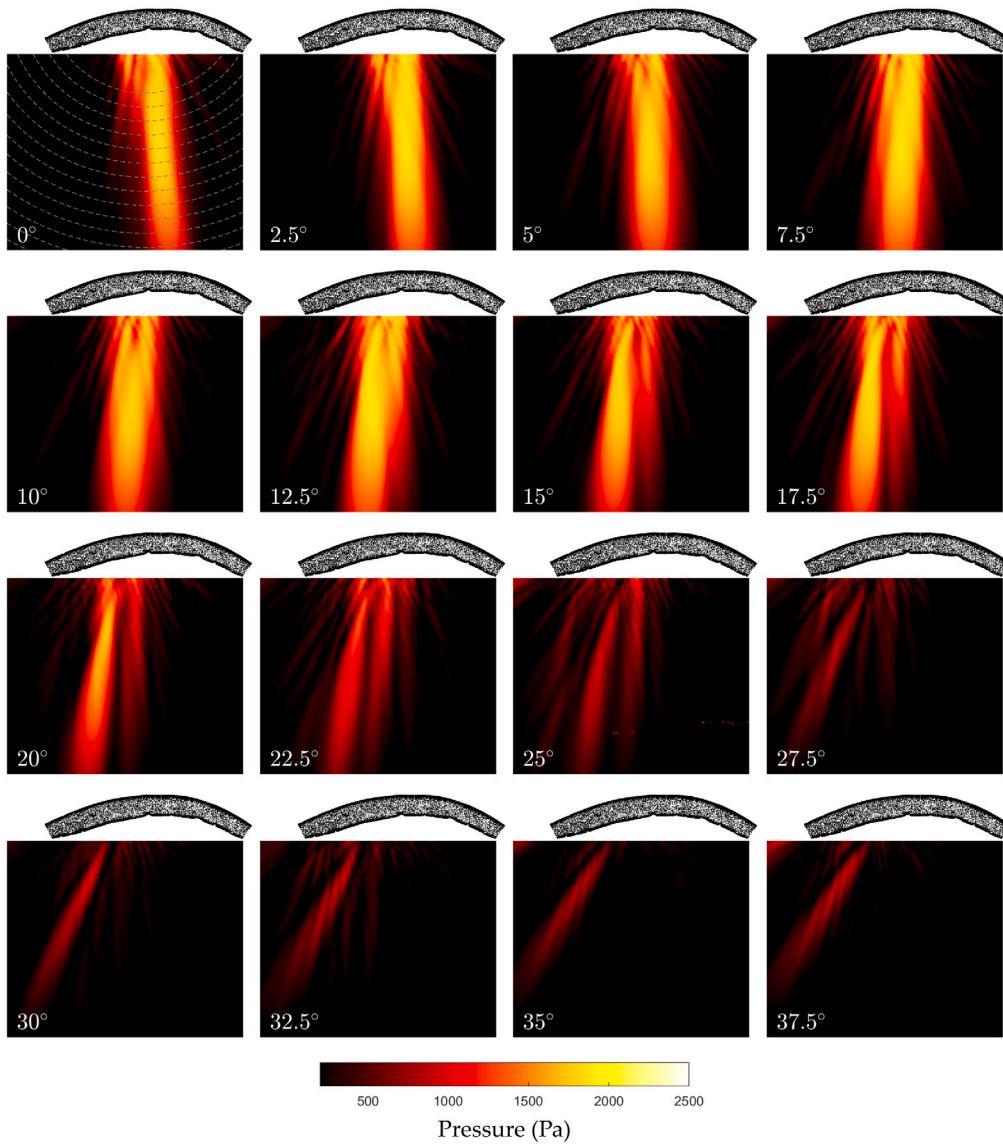
Fig. 6. Root Mean Square (RMS) maps of the experimental pressure field $p(x_1, x_2, t)$ for the parietal bone of Fig. 1(b).
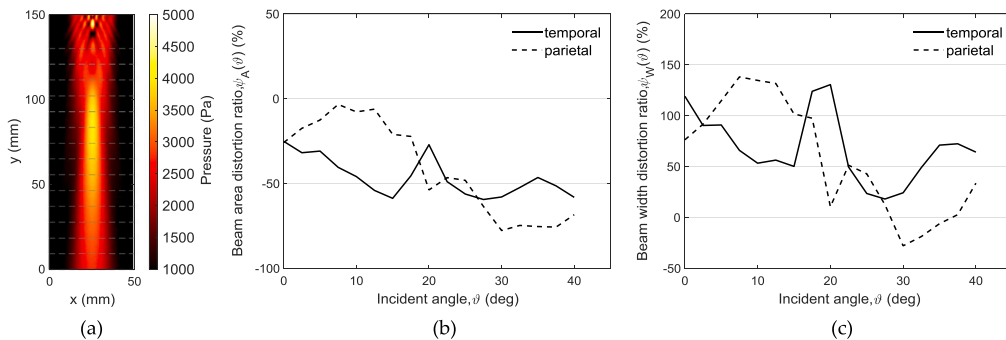
Fig. 7. (a) Free field RMS map of the acoustic pressure generated by the immersion transducer at 500 kHz. (b) Beam area and (c) beam width distortion ratio with respect to the free field.

confirms that immersed setups at large incidence angles can potentially achieve better spatial resolution.

4.2. Radiation tests

In the radiation tests, the transducer was positioned near the edge of the cranial bones as indicated in Fig. 4(b) and excited with a broadband signal consisting of a 1.5-cycles Gaussian-modulated sine wave with 500 kHz central frequency. With this transducer configuration, different leaky guided wave modes are excited, whose corresponding radiated pressure field can be recognized in the time snapshot Fig. 4(b) as they separate from the main direct wave. Since the acoustic energy carried by the direct wave is substantially larger than that of the radiated
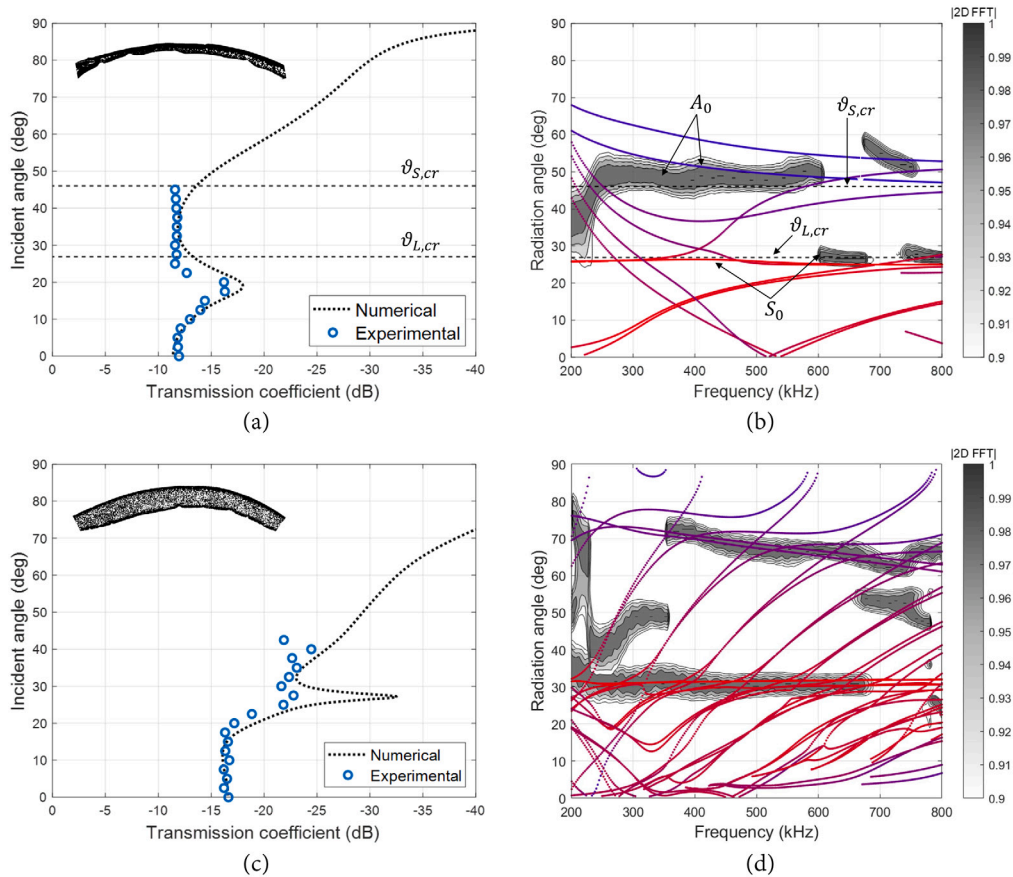
Fig. 8. Experimental peak transmission coefficients $T^{(p)}(f, \vartheta)$ versus numerical plane wave transmission coefficients $T(f, \vartheta)$ for the (a) temporal and (c) parietal bone at 500 kHz. Experimental versus numerical radiation angle dispersion curves for the (b) temporal and (d) parietal bone in the 200–800 kHz range.

leaky waves, the computation of the frequency-dependent radiation angles associated to different leaky modes is carried over a sub-window of the 2D scan region (dotted line in Fig. 4(b)) that excludes the direct wave. Following the approach of Refs. [21,25], the experimental frequency-radiation angle $(f - \vartheta)$ dispersion diagrams are obtained by first applying a cosine-tapered (Tukey) window in time and space to the 3D pressure field array $p(x_1, x_2, t)$ recorded over the sub-window. This array is then Fourier-transformed from the time-space domain (x_1, x_2, t) to the frequency–wavenumber domain (k_1, k_2, f). In order to reduce the Fourier-transformed 3D pressure array $P(k_1, k_2, f)$ to a 2D array that can be used to evaluated the frequency-radiation angle $(f - \vartheta)$ dispersion map of the cranial bone, the change of variable $\vartheta = \tan^{-1}[\text{Re}(k_1(f))/\text{Re}(k_2(f))]$ is applied at any discrete frequency f, which contracts the two-dimensional space $(k_1(f), k_2(f))$ to the one-dimensional space $\vartheta(f)$. Repeating this operation for all the discrete frequencies in the array yields the 2D array $P(\vartheta, f)$, which is shown in Figs. 8(b) and 8(d) for the temporal and parietal bone, respectively

4.3. Comparison against numerical results

The transmission curves $\vartheta_i - T^{(p)}(\vartheta_i, f = 500 \text{ kHz})$ and dispersion spectra $f - \vartheta$ determined experimentally are shown in Fig. 8. As mentioned in Section 2, the transmission curves were first used to calibrate the attenuation coefficients α_L and α_S reported in Table 1, which were then employed in the transmission and radiation numerical analyses. It is noted that, since scattering cannot directly be accounted for in the matrix propagator and Semi-Analytical Finite Element models, its effect is implicitly accounted for in α_L and α_S.

For the case of the temporal bone, the numerical and experimental transmission curve at 500 kHz are in very good agreement. As it can be

noted, in the range $\vartheta_i \in [\vartheta_{L,cr}, \vartheta_{S,cr}]$ the measured transmission coefficient is only slightly higher with respect to the normal incidence case. A global overview of the acoustic energy distribution at different incident angles in the intracranial region can be obtained from the inspection of Fig. 5, where the highest RMS values are observed at angles $\vartheta_i > 25°$. It is also worth noting that the transmitted acoustic beam is less distorted in the range $\vartheta_i \in [25°, 35°]$ with respect to the range $\vartheta_i \in [0°, 5°]$ (normal incidence) due to the more efficient shear mode conversion, which results in less refraction and therefore less pronounced side lobes. By looking at the frequency-radiation spectrum of Section 4.3(b), it clearly appears that the two critical angles are intercepted by the fundamental modes S_0 and A_0 (shaded areas in gray scale), which are in turn overlapped by the corresponding numerical dispersion curves. These results validate the conclusions draw in Section 3.3.1, based on which the Snell's critical angles can be approximated sufficiently well by using the $f - \vartheta$ spectrum derived via pure signal processing, and that efficient transmission and lower beam distortion can be achieved within the range defined by these angles. As an additional remark, the knowledge of the first critical angle can be helpful in determining the range of incident angles that can be potentially associated to low transmission. The latter can be expected for up to 10° below $\vartheta_{L,cr}$, as demonstrated by the dip in the experimental transmission curve (Fig. 8(a)) and numerical transmission map (Fig. 2(d)).

Similar results can also be observed for the parietal bone. Also in this case, the numerical and experimental transmission curves are in good agreement except in the range $\vartheta_i \in [25°, 30°]$, where the numerical curve exhibits a sharp dip that is not well captured by the experimental one. The reason of such discrepancy is mainly due to the assumptions made in the numerical modeling, where incident

monochromatic waves are used. A better fit would be achieved by adopting a more realistic modeling approach such as that in [33–35], where the effects of the finite width of the incident beam are considered, although this is beyond scope of this work. The comparison between the experimental transmission data of Fig. 8(c), the radiation data of Fig. 8(d) and the RMS plots of Fig. 6 shows that also in this case the cluster of longitudinally polarized modes (here located at $\vartheta_i = 30°$) can be obtained by pure signal processing and employed to determine the virtual boundary that separates regions of low transmission (below the cluster) from regions of lower beam distortion (above the cluster). In fact, it can be noted from Fig. 6 that the latter is greatly improved at incident angles above $\vartheta_i = 30°$ with respect to the normal incidence case, even though the transmitted peak pressure is quite reduced. In order to verify if high levels of transmission can be achieved at incident angles larger than that determined by the cluster of longitudinally polarized modes, additional tests should be conducted on parietal bones with different sizes and mechanical properties. Some studies have been recently proposed in this sense, where the transmitted acoustic power has been shown to be drastically reduced in bone phantoms with larger trabecular thickness and level of porosity [38,39], which appears to be consistent with the findings of this work.

5. Conclusions

We investigated the relation between the transcranial ultrasound transmission of a temporal and a parietal bone and its connection to the mode conversion phenomena that take place at the bone–fluid interface for a varying incident angle. The key result of this study is that the frequency-radiation angle dispersion spectrum of cranial leaky guided waves can be used to evaluate the range of incident angles within which efficient longitudinal-to-shear mode conversion is achieved at the bone–fluid interface. Leveraging this effect can ultimately lead to lower distortions on the transmitted acoustic beam and, consequently, better spatial resolution in the intracranial region. This finding is demonstrated both experimentally and numerically through transmission and dispersion analyses. Specifically, the experimental transmission coefficient measured for a temporal and parietal bone at 500 kHz and for incident angles spanning 0°–45° shows a good agreement with the numerical solution given by a matrix propagator approach, which is also used to derive the numerical frequency-incident angle transmission map of the two bones in the 200–800 kHz range. The comparison of these maps with the experimental dispersion data and its numerical counterpart computed with a Semi-Analytical Finite Element approach revealed that the first critical incident angle corresponds to the radiation angle associated to longitudinally-polarized leaky guided wave modes. Both experimental and numerical data confirmed that, above this angle, lower beam distortions are observed for both bones, with the temporal bone also leading to slightly better transmission coefficients with respect to the normal incidence case. At 5°–10° below this angle, transmission drops are likely to be expected in the sub-1.0 MHz regime, regardless of the type of cranial bone. Since the dispersion characteristics of leaky guided waves can be obtained by pure signal processing procedure, the critical angles for the sonicated skull region can be estimated without a prior knowledge of the geometric and mechanical properties of the skull bone.

The results presented in this study can be useful in the design of transcranial ultrasound setups that seek to target confined regions of the brain, and in setups that leverage inclined dual transducer configurations.

Declaration of competing interest

The authors declare that they have no known competing financial interests or personal relationships that could have appeared to influence the work reported in this paper.

Data availability

Data will be made available on request.

Appendix A. Bone density measurement

The cortical and trabecular densities ρ_c and ρ_t of a given skull segment are calculated using an expression relating the total measured bone mass to the total numerical mass estimated for the reconstructed cortical bone and trabecular layers, which is in turn performed by means of the reconstruction algorithm described in [22]. Since the bone density is linearly proportional to the Hounsfield Units (HU) in the μCT scans, the ratio between the cortical and trabecular densities is linearly related to the corresponding average HU ratio (HU_c/HU_d) in the bone regions. As a consequence, the following relations hold:

$$\rho_c V_c + \rho_t V_t = m_b, \tag{A.1}$$

$$\rho_c/\rho_t = HU_c/HU_t, \tag{A.2}$$

where $V_{c,t}$ are the numerically reconstructed cortical and trabecular volumes, while m_b is the measured total mass of the bone segment. The densities ρ_c and ρ_t are directly obtained by solving Eqs. (A.1) and (A.2).

Appendix B. Analytical coefficients

The analytical expressions of the coefficients $s_{ij}^{(l)}$ for the lth layer are [24]:

$$s_{11}^{(l)} = G_l \cos P_l + \left(1 - G_l\right) \cos Q_l,$$
$$s_{12}^{(l)} = i\left[\left(1 - G_l\right) \sin P_l/E_l\right] - iF_l G_l \sin Q_l,$$
$$s_{13}^{(l)} = -\left(1/H_l\right)\left(\cos P_l - \cos Q_l\right),$$
$$s_{14}^{(l)} = -\left(i/H_l\right)\left[\sin P_l/E - l + F_l \sin Q_l\right],$$
$$s_{21}^{(l)} = iE_l G_l \sin P_l - i\left[\left(1 - G_l\right) \sin Q_l\right]/F_l,$$
$$s_{22}^{(l)} = \left(1 - G_l\right) \cos P_l + G_l \cos Q_l,$$
$$s_{23}^{(l)} = -\left(i/H_l\right)\left(E_l \sin P_l + \sin Q_l/F_l\right),$$
$$s_{24}^{(l)} = s_{13}^{(l)},$$
$$s_{31}^{(l)} = -H_l G_l \left(1 - G_l\right)\left(\cos P_l - \cos Q_l\right),$$
$$s_{32}^{(l)} = -iH_l \left\{\left[\left(1 - G_l\right)^2 \sin P_l\right]/E_l + F_l G_l^2 \sin Q_l\right\},$$
$$s_{33}^{(l)} = s_{22}^{(l)},$$
$$s_{34}^{(l)} = s_{12}^{(l)},$$
$$s_{41}^{(l)} = -iH_l \left\{E_l G_l^2 \sin P_l + \left[\left(1 - G_l\right)^2 \sin Q_l\right]/F_l\right\},$$
$$s_{42}^{(l)} = s_{31}^{(l)},$$
$$s_{43}^{(l)} = s_{21}^{(l)},$$
$$s_{44}^{(l)} = s_{11}^{(l)},$$

in which the different quantities are given by

$$P_l = k_{z,L}^{(l)} t^{(l)}, \; Q_l = k_{z,S}^{(l)} t^{(l)}, \; E_l = k_{z,L}^{(l)}/k_x, \; F_l = k_{z,S}^{(l)}/k_x,$$
$$G_l = 2k_x^2/(k_S^{(l)})^2, \; H_l = \rho^{(l)}\omega/k_x,$$

where

$$k_{z,L}^{(l)} = [(k_L^{(l)})^2 - k_x^2]^{1/2}, \quad k_{z,S}^{(l)} = [(k_S^{(l)})^2 - k_x^2]^{1/2}. \tag{B.1}$$

are complex transverse wavenumbers. In Eq. (B.1), the complex wavenumbers $k_L^{(l)}$ and $k_S^{(l)}$ for the longitudinal and shear waves within the lth layer are expressed as $k_{L,S}^{(l)} = \omega/c_{L,S}^{(l)}$, in which $c_{L,S}$ are the corresponding complex phase speeds. The latter are obtained from the relation

$$c_{L,S}^{(l)} = \frac{\tilde{c}_{L,S}^{(l)}}{1 + i\alpha_{L,S}^{(l)} \tilde{c}_{L,S}^{(l)}/(2\pi)},$$

in which $\alpha_{L,S}^{(l)}$ and $\tilde{c}_{L,S}^{(l)}$ denote the attenuation and phase speed of longitudinal and shear bulk waves, respectively.

Appendix C. Semi-analytical finite element approach for the $k_x(f)$ and $f(k_x)$ formulations.

The Semi-Analytical Finite Element (SAFE) approach used to study the dispersion properties of the cranial bone is similar to that described in [20,21]. The method consists in assuming a propagation process with a space and time dependence of the form $\exp[i(k_x x - 2\pi f t)]$ and discretizing the bone along the z-direction by using a one-dimensional mesh of n finite elements. Following [21], a sixth order polynomial eigenvalue problem for the $k_x(f)$ formulation can be written in the form

$$\left[\sum_{j=0}^{6} \gamma^j(f)\boldsymbol{\Gamma}_j(f)\right]\boldsymbol{\Phi}(f) = \mathbf{0}, \tag{C.1}$$

where $\boldsymbol{\Gamma}_j(f)$ is a dynamic stiffness matrix, $\boldsymbol{\Phi}(f)$ is an eigenvector containing the displacement components of the guided wave mode at any node of the finite element mesh while $\gamma(f)$ is the associated complex eigenvalue such that $k_x(f) = k_f(f)[\gamma(f) + \gamma^{-1}(f)]/2$. The matrix operators in Eq. (C.1) are expressed as

$\boldsymbol{\Gamma}_0(f) = ik_f^3(f)\mathbf{K}_3,$

$\boldsymbol{\Gamma}_1(f) = -2k_f^2(f)(\mathbf{K}_2 - \mathbf{K}_2^{\mathrm{T}}),$

$\boldsymbol{\Gamma}_2(f) = ik_f^3(f)\mathbf{K}_3 + 4ik_f(f)\left(\mathbf{K}_1 - \pi^2 f^2 \mathbf{M}\right),$

$\boldsymbol{\Gamma}_3(f) = 32i\pi^2 f^2 \rho_f \mathbf{Q},$

$\boldsymbol{\Gamma}_4(f) = -ik_f^3(f)\mathbf{K}_3 - 4ik_f(f)\left(\mathbf{K}_1 - \pi^2 f^2 \mathbf{M}\right),$

$\boldsymbol{\Gamma}_5(f) = 2k_f^2(f)(\mathbf{K}_2 - \mathbf{K}_2^{\mathrm{T}}),$

$\boldsymbol{\Gamma}_6(f) = -ik_f^3(f)\mathbf{K}_3,$

in which the stiffness, mass and fluid coupling matrices are given by

$$\mathbf{K}_1 = \mathop{\mathbf{A}}_{e=1}^{n} \int_{l_e} [\partial_z \mathbf{N}(z)]^{\mathrm{T}} \mathbf{C}(f,z)\partial_z \mathbf{N}(z)z,$$

$$\mathbf{K}_2 = \mathop{\mathbf{A}}_{e=1}^{n} \int_{l_e} [\partial_{x_3} \mathbf{N}(x_3)]^{\mathrm{T}} \mathbf{C}(f,z)\partial_x \mathbf{N}(z)z,$$

$$\mathbf{K}_3 = \mathop{\mathbf{A}}_{e=1}^{n} \int_{l_e} [\partial_x \mathbf{N}(x_3)]^{\mathrm{T}} \mathbf{C}(f,z)\partial_x \mathbf{N}(z)z,$$

$$\mathbf{M} = \mathop{\mathbf{A}}_{e=1}^{n} \int_{l_e} [\mathbf{N}(z)]^{\mathrm{T}} \rho(z)\mathbf{N}(z)z,$$

$$\mathbf{Q} = \mathop{\mathbf{A}}_{e=1}^{n} \begin{bmatrix} 0 & 0 \\ 0 & s \end{bmatrix},$$

where $\mathop{\mathbf{A}}_{e=1}^{n}$ indicates a matrix assembly operation in the direct stiffness sense, $s = 1$ if $e = 1$ or $e = n$ ($s = 0$ otherwise), $\mathbf{N}(z)$ is a matrix of polynomial shape functions, $\rho(z)$ and $\mathbf{C}(f,z)$ denote the density and fourth order tensor of elastic moduli of the cortical bone, respectively,

while

$$\partial_z = \begin{bmatrix} 0 & 0 & 0 \\ 0 & 0 & 0 \\ 0 & 0 & \frac{\partial}{\partial z} \\ 0 & \frac{\partial}{\partial z} & 0 \\ \frac{\partial}{\partial z} & 0 & 0 \\ 0 & 0 & 0 \end{bmatrix}, \quad \partial_x = \begin{bmatrix} 1 & 0 & 0 \\ 0 & 0 & 0 \\ 0 & 0 & 0 \\ 0 & 0 & 0 \\ 0 & 0 & 1 \\ 0 & 1 & 0 \end{bmatrix},$$

are compatibility operators.

When the eigenset $[\gamma_k(f), \boldsymbol{\Phi}_k(f)]$ for the kth guided wave modes has been extracted from Eq. (C.1) for a fixed frequency f and given material properties, the angle $\vartheta_k(f)$ at which the same mode radiates energy into the surrounding fluid (see Fig. 1(c)) can be extracted from the generalized Snell's law using the relation

$$\vartheta_k(f) = \sin^{-1}\left[\frac{\mathrm{Re}[k_{x,k}(f)]}{k_f(f)}\right] = \sin^{-1}\left[\frac{\mathrm{Re}[\gamma_k(f) + \gamma_k^{-1}(f)]}{2}\right]. \tag{C.2}$$

In the $f(k_x)$ formulation, the fundamental relation $k_x = \omega/c_p$ between angular frequency $\omega = 2\pi f$, wavenumber k_x and phase velocity c_p of a given guided wave mode is used to reduce the dispersion equation to the standard second order polynomial eigenvalue problem

$$\left[\omega^2(c_p)\left(\frac{\mathbf{K}_3}{c_p^2} - \mathbf{M}\right) + i\omega(c_p)\left(\frac{\mathbf{K}_2}{c_p} + \frac{\rho_f}{\sqrt{c_f^{-2} - c_p^{-2}}}\mathbf{Q}\right) + \mathbf{K}_1\right]\boldsymbol{\Phi}(c_p) = \mathbf{0},$$

which can be solved for $\omega(c_p)$ when c_p is a real valued fixed parameter. From the computed eigensets $[\omega_k(c_p), \boldsymbol{\Phi}_k(c_p)]$, the corresponding quantities $[f_k(k_x), \boldsymbol{\Phi}_k(k_x)]$ can be readily derived, from which the radiation angle can be finally computed as in Eq. (C.2).

The polarization factor $PF_k(f)$ used to encode the curves in Figs. 2 and 3 takes values from 0 (longitudinally polarized modes) to 1 (transversally polarized modes), and is post-processed for the kth leaky guided wave mode from the corresponding numerical eigenvector $\boldsymbol{\Phi}_k$ as

$$PF_k = \frac{\int_0^H |\boldsymbol{\Phi}_k| \cdot \mathbf{p}_z^{\mathrm{T}} dz}{\int_0^H \|\boldsymbol{\Phi}_k\|_2 dz},$$

where $\mathbf{p}_z$ is a logical vector that evaluates the degrees of freedom along the z-direction.

References

[1] S. Kim, Y. Jo, G. Kook, C. Pasquinelli, H. Kim, K. Kim, H.-S. Hoe, Y. Choe, H. Rhim, A. Thielscher, J. Kim, H.J. Lee, Transcranial focused ultrasound stimulation with high spatial resolution, Brain Stimul. 14 (2021) 290–300, http://dx.doi.org/10.1016/j.brs.2021.01.002, https://www.sciencedirect.com/science/article/pii/S1935861X21000036.

[2] G.T. Clement, P.J. White, K. Hynynen, Enhanced ultrasound transmission through the human skull using shear mode conversion, J. Acoust. Soc. Am. 115 (2004) 1356–1364, http://dx.doi.org/10.1121/1.1645610.

[3] P. White, G. Clement, K. Hynynen, Longitudinal and shear mode ultrasound propagation in human skull bone, Ultrasound Med. Biol. 32 (2006) 1085–1096, http://dx.doi.org/10.1016/j.ultrasmedbio.2006.03.015.

[4] F. Vignon, W.T. Shi, X. Yin, T. Hoelscher, J.E. Powers, The stripe artifact in transcranial ultrasound imaging, J. Ultrasound Med. 29 (2010) 1779–1786, http://dx.doi.org/10.7863/jum.2010.29.12.1779.

[5] S. Pichardo, K. Hynynen, Treatment of near-skull brain tissue with a focused device using shear-mode conversion: a numerical study, Phys. Med. Biol. 52 (2007) 7313–7332, http://dx.doi.org/10.1088/0031-9155/52/24/008.

[6] S. Pichardo, C. Moreno-Hernádez, R.A. Drainville, V. Sin, L. Curiel, K. Hynynen, A viscoelastic model for the prediction of transcranial ultrasound propagation: application for the estimation of shear acoustic properties in the human skull, Phys. Med. Biol. 62 (2017) 6938–6962, http://dx.doi.org/10.1088/1361-6560/aa7ccc.

[7] J.K. Mueller, L. Ai, P. Bansal, W. Legon, Numerical evaluation of the skull for human neuromodulation with transcranial focused ultrasound, J. Neural Eng. 14 (2017) 066012, http://dx.doi.org/10.1088/1741-2552/aa843e.

[8] D. Modena, M. Baragona, D. Bošnački, B.J.T. Breuer, A. Elevelt, R.T.H. Maessen, P.A.J. Hilbers, H.M.M. ten Eikelder, Modeling the interference between shear and longitudinal waves under high intensity focused ultrasound propagation in bone, Phys. Med. Biol. 63 (2018) 235024, http://dx.doi.org/10.1088/1361-6560/aaef14.

[9] H. Montanaro, C. Pasquinelli, H.J. Lee, H. Kim, H.R. Siebner, N. Kuster, A. Thielscher, E. Neufeld, The impact of CT image parameters and skull heterogeneity modeling on the accuracy of transcranial focused ultrasound simulations, J. Neural Eng. 18 (2021) 046041, http://dx.doi.org/10.1088/1741-2552/abf68d.

[10] M.A. Samoudi, T.V. Renterghem, D. Botteldooren, Computational modeling of a single-element transcranial focused ultrasound transducer for subthalamic nucleus stimulation, J. Neural Eng. 16 (2019) 026015, http://dx.doi.org/10.1088/1741-2552/aafa38.

[11] C. Pasquinelli, H. Montanaro, H.J. Lee, L.G. Hanson, H. Kim, N. Kuster, H.R. Siebner, E. Neufeld, A. Thielscher, Transducer modeling for accurate acoustic simulations of transcranial focused ultrasound stimulation, J. Neural Eng. 17 (2020) 046010, http://dx.doi.org/10.1088/1741-2552/ab98dc.

[12] R.M. Jones, M.A. O'Reilly, K. Hynynen, Transcranial passive acoustic mapping with hemispherical sparse arrays using CT-based skull-specific aberration corrections: a simulation study, Phys. Med. Biol. 58 (2013) 4981–5005, http://dx.doi.org/10.1088/0031-9155/58/14/4981.

[13] R.M. Jones, K. Hynynen, Comparison of analytical and numerical approaches for CT-based aberration correction in transcranial passive acoustic imaging, Phys. Med. Biol. 61 (2015) 23–36, http://dx.doi.org/10.1088/0031-9155/61/1/23.

[14] J. Peterson, P.C. Dechow, Material properties of the human cranial vault and zygoma, Anat. Rec. Part A: Discov. Mol. Cell. Evol. Biol. 274A (2003) 785–797, http://dx.doi.org/10.1002/ar.a.10096.

[15] A. Wydra, E. Malyarenko, K. Shapoori, R.G. Maev, Development of a practical ultrasonic approach for simultaneous measurement of the thickness and the sound speed in human skull bones: a laboratory phantom study, Phys. Med. Biol. 58 (2013) 1083–1102, http://dx.doi.org/10.1088/0031-9155/58/4/1083.

[16] K. Firouzi, P. Ghanouni, B.T. Khuri-Yakub, Efficient transcranial ultrasound delivery via excitation of lamb waves: Concept and preliminary results, in: 2017 IEEE International Ultrasonics Symposium, IUS, IEEE, 2017, pp. 1–4.

[17] H. Estrada, J. Rebling, D. Razansky, Prediction and near-field observation of skull-guided acoustic waves, Phys. Med. Biol. 62 (2017) 4728–4740, http://dx.doi.org/10.1088/1361-6560/aa63e3.

[18] H. Estrada, S. Gottschalk, M. Reiss, V. Neutschmelting, R. Goldbrunner, D. Razansky, Observation of guided acoustic waves in a human skull, Ultrasound Med. Biol. 44 (2018) 2388–2392, http://dx.doi.org/10.1016/j.ultrasmedbio.2018.05.019.

[19] H. Estrada, S. Gottschalk, M. Reiss, V. Neuschmelting, J. Rebling, R. Goldbrunner, D. Razansky, Looking at the skull in a new light: Rayleigh-lamb waves in cranial bone, in: 2018 IEEE International Ultrasonics Symposium, IUS, 2018, pp. 1–3.

[20] M. Mazzotti, C. Sugino, E. Kohtanen, A. Erturk, M. Ruzzene, Experimental identification of high order lamb waves and estimation of the mechanical properties of a dry human skull, Ultrasonics 113 (2021) 106343, http://dx.doi.org/10.1016/j.ultras.2020.106343.

[21] M. Mazzotti, E. Kohtanen, A. Erturk, M. Ruzzene, Radiation characteristics of cranial leaky lamb waves, IEEE Trans. Ultrason. Ferroelectr. Freq. Control 68 (2021) 2129–2140, http://dx.doi.org/10.1109/TUFFC.2021.3057309.

[22] E. Kohtanen, M. Mazzotti, A. Erturk, Vibration-based elastic parameter identification of the diplo and cortical tables in dry cranial bones, J. Mech. Behav. Biomed. Mater. 123 (2021) 104747, http://dx.doi.org/10.1016/j.jmbbm.2021.104747.

[23] L. Brekhovskikh, O. Godin, Acoustic of layered media 1, in: Plane and Quasi-Plane Waves, second ed., Springer-Verlag, Berlin, 1990.

[24] D.L. Folds, C.D. Loggins, Transmission and reflection of ultrasonic waves in layered media, J. Acoust. Soc. Am. 62 (1977) 1102–1109, http://dx.doi.org/10.1121/1.381643.

[25] E. Kohtanen, M. Mazzotti, M. Ruzzene, A. Erturk, Radiation characterization of leaky guided waves in monolithic and sutured cranial bones, in: 2021 IEEE International Ultrasonics Symposium, IUS, 2021, pp. 1–3, http://dx.doi.org/10.1109/IUS52206.2021.9593309.

[26] E. Kohtanen, M. Mazzotti, M. Ruzzene, A. Erturk, Transcranial radiation characteristics of leaky lamb waves in different regions of a human skull, J. Acoust. Soc. Am. 149 (2021) A18, http://dx.doi.org/10.1121/10.0004390.

[27] M. Deschamps, O. Poncelet, Transient lamb waves: Comparison between theory and experiment, J. Acoust. Soc. Am. 107 (2000) 3120–3129, http://dx.doi.org/10.1121/1.429341.

[28] W.T. Thomson, Transmission of elastic waves through a stratified solid medium, J. Appl. Phys. 21 (1950) 89–93, http://dx.doi.org/10.1063/1.1699629.

[29] B. Pavlakovic, M.J.S. Lowe, D.N. Alleyne, P. Cawley, Disperse: A General Purpose Program for Creating Dispersion Curves, Vol. 16, Plenum Press, New York, 1997, pp. 185–192.

[30] M. Mazzotti, I. Bartoli, A. Marzani, E. Viola, A coupled safe-2.5d bem approach for the dispersion analysis of damped leaky guided waves in embedded waveguides of arbitrary cross-section, Ultrasonics 53 (2013) 1227–1241.

[31] M. Mazzotti, A. Marzani, I. Bartoli, Dispersion analysis of leaky guided waves in fluid-loaded waveguides of generic shape, Ultrasonics 54 (2014) 408–418.

[32] M. Mazzotti, A. Marzani, I. Bartoli, E. Viola, Guided waves dispersion analysis for prestressed viscoelastic waveguides by means of the safe method, Int. J. Solids Struct. 49 (2012) 2359–2372.

[33] T. Ngoc, W. Mayer, A general description of ultrasonic nonspecular reflection and transmission effects for layered media, IEEE Trans. Sonics Ultrason. 27 (1980) 229–235, http://dx.doi.org/10.1109/T-SU.1980.31182.

[34] K. Van Den Abeele, O. Leroy, On the influence of frequency and width of an ultrasonic bounded beam in the investigation of materials: Study in terms of heterogeneous plane waves, J. Acoust. Soc. Am. 93 (1993) 2688–2699, http://dx.doi.org/10.1121/1.405844.

[35] K. Van Den Abeele, O. Leroy, Complex harmonic wave scattering as the framework for investigation of bounded beam reflection and transmission at plane interfaces and its importance in the study of vibrational modes, J. Acoust. Soc. Am. 93 (1993) 308–323, http://dx.doi.org/10.1121/1.405665.

[36] R. Fiorito, W. Madigosky, H. Überall, Resonance theory of acoustic waves interacting with an elastic plate, J. Acoust. Soc. Am. 66 (1979) 1857–1866, http://dx.doi.org/10.1121/1.383618.

[37] D.E. Chimenti, S.I. Rokhlin, Relationship between leaky lamb modes and reflection coefficient zeroes for a fluid-coupled elastic layer, J. Acoust. Soc. Am. 88 (1990) 1603–1611, http://dx.doi.org/10.1121/1.400319.

[38] B. Jing, B.D. Lindsey, Effect of skull porous trabecular structure on transcranial ultrasound imaging in the presence of elastic wave mode conversion at varying incidence angle, Ultrasound Med. Biol. 47 (2021) 2734–2748, http://dx.doi.org/10.1016/j.ultrasmedbio.2021.05.010.

[39] B. Jing, M. Mazzotti, M. Ruzzene, B.D. Lindsey, Skull microstructure and mode conversion in transcranial ultrasound imaging, in: 2021 IEEE International Ultrasonics Symposium, IUS, 2021, pp. 1–4, http://dx.doi.org/10.1109/IUS52206.2021.9593639.